(NASA-TM-103481) EARTH RADIATION BUDGET EXPERIMENT (ERBE) VALIDATION (NASA) 59 p
CSCL 04A
N90-26433
Unclas
G3/46 0292257

EARTH RADIATION BUDGET EXPERIMENT (ERBE) VALIDATION

Bruce R. Barkstrom, Edwin F. Harrison, G. Louis Smith,

Richard N. Green, and James F. Kibler

Atmospheric Sciences Division, NASA Langley Research Center

Hampton, VA 23665-5225

Robert D. Cess

Laboratory for Planetary and Atmospheric Sciences

State University of New York at Stony Brook

Stony Brook, NY 91537

The ERBE Science Team*

* ERBE Science Team principal investigators: B. R. Barkstrom, ERBE Experiment Scientist and Science Team Leader, Atmospheric Sciences Division, NASA Langley Research Center; R. D. Cess, State University of New York at Stony Brook; J. A. Coakley Jr., Oregon State University; Y. Fouquart, LOA, University of Lille, France; A. Gruber, NOAA NESDIS; D. L. Hartmann, University of Washington, Seattle; E. F. Harrison, NASA Langley Research Center; F. B. House, Drexel University; R. S. Kandel, LMD, CNRS, Palaiseau, France; M. D. King, ERBE Project Scientist, NASA Goddard Space Flight Center; A. T. Mecherikunnel, NASA Goddard Space Flight Center; A. J. Miller, NOAA NMC; V. Ramanathan, University of Chicago; E. Raschke, University of Köln,

Introduction to ERBE Data

During the past 4 years, data from the Earth Radiation Budget Experiment (ERBE) have been undergoing detailed examination [Barkstrom and Smith, 1986; Barkstrom, 1984; ERBE Science Team, 1986]. There is no direct source of "groundtruth" for the radiation budget. Thus, this validation effort has had to rely heavily upon intercomparisons between different types of measurements. The ERBE Science Team chose 10 measures of agreement as validation criteria. Late in August 1988, the Team agreed that the data met these conditions. As a result, the final, monthly averaged data products are being archived. This paper describes these products, their validation, and some results for January 1986. The paper also provides information on obtaining the data from the archive.

Instrument Overview

Three satellites collect the ERBE data. These satellites are the Earth Radiation Budget Satellite (ERBS), NOAA-9, and NOAA-10. Space Shuttle Challenger launched ERBS on October 4, 1984. Over the week after launch, this satellite ascended from the Challenger's altitude to its operational altitude of about 600 km. Absolute calibration requires avoiding as much contamination as possible. The ERBE instruments avoided contaminants by keeping their covers closed during the first month in orbit. Thus, earth-viewing data collection from the ERBS instruments began on November 5, 1984. The NOAA instruments also kept their covers closed for the first month in orbit. Earth-viewing

FRG; G. L. Smith, NASA Langley Research Center; W. L. Smith, University of Wisconsin, Madison; and T. H. Vonder Haar, Colorado State University. [Barkstrom, 1984] lists the complete ERBE Science Team.

data collection on NOAA-9 began January 5, 1985; on NOAA-10, it began November 12, 1986. At present, the ERBE instruments on all three satellites continue to send data to earth. The scanner on NOAA-9 ceased data transmission in January 1987, after it exceeded its design goal of 2 years of operation. This is the only significant data loss so far.

The article by Kopia [1986] describes the scanner package. This instrument has three telescopes which are "bore-sighted" to provide more than 98 % overlap of the fields of view. The three channels provide radiances in very broad spectral bands. The total (TOT) channel observes from 0.15 μm to wavelengths greater than 200 μm. The shortwave (SW) is sensitive to wavelengths from 0.2 μm to about 4.5 μm. The longwave (LW) is sensitive from about 6 μm to about 35 μm. The Point Spread Function (PSF) of these instruments is roughly a 2-dimensional Gaussian shape. The half-power point has an angular diameter of about 3.7 ° [Huck et al., 1981]. For the ERBS, this gives a circular footprint with a diameter of 40 km at nadir. The scanners have usually operated in a crosstrack mode. A single channel provides 62 samples of radiances from the earth every 4 seconds. Thus, over the course of a day, each channel of a scanner provides about 1.3 million pixels.

The nonscanner package contains the "classic" earth radiation budget instruments: a pair of wide field-of-view (WFOV), "flat plate" radiometers. These see a circular portion of the earth from limb to limb. This package also contains a pair of medium field-of-view (MFOV) instruments. These see an area about 1000 km in diameter. Finally, the nonscanner package carries a solar monitor that is essentially the same as those on the Solar Maximum Mission [Willson, 1979]. Luther et al. [1986] provide details of these instruments' design and operation. The pairs of channels for each resolution provide simultaneous observations of the total spectrum and of its shortwave part. Quantitatively,

the shortwave (SW) part of the spectrum ranges from 0.2 μm to about 4.5 μm. The total spectrum covers the range from 0.15 μm to longer than 200 μm. The nonscanner microprocessor samples the signals from each channel every 0.8 seconds. This sampling gives about 108,000 measurements per day per channel.

Data Processing Overview

It is convenient to think of the work of data processing as falling into three parts. The first is interpreting the instrument data. The second is computing the top-of-the-atmosphere fluxes. The third is averaging over time and space.

The instrument processing involves two subtasks. The first is "merge and locate." The second is "count conversion." These names are fairly descriptive. The satellite location and velocity are not in the same data stream as the telemetry data from the instruments. Therefore, the ephemeris data (with satellite location and velocity) must be merged with the telemetry data. Then, the processing system must compute the colatitude and longitude where each channel's observations intersect the top of the atmosphere. The two geometric coordinates are the field-of-view location. The second subtask is to convert the instrument telemetry (in counts) to radiometric units. For the scanners, the unit is filtered radiance, which has dimensions $\mathrm{W\,m^{-2}\,sr^{-1}}$. By filtered, we mean that the dimensionless spectral coloration of the instrument is still included in the measurement. For the nonscanners, the radiometric unit is the irradiance of the sensor, which has dimensions $\mathrm{W\,m^{-2}}$.

The top-of-the-atmosphere (TOA) flux computation takes its name from the equations for the nonscanners. These are similar to those for atmospheric profile inversion, e.g.,

[Twomey, 1977]. Thus, this second step in the ERBE processing is "inversion." The problem for the ERBE nonscanners is more complex because the equations are 2-dimensional Fredholm integral equations of the first kind. Nonetheless, the solution techniques for atmospheric profile inversion apply to the data interpretation.

The averaging process also has several steps. The first step is producing averages of instantaneous data within geographic regions. The second is breaking the single time series from a satellite into separate time series for each region. If a second satellite has observed a region during the month, the third step is merging the two regional time series. Finally, the time series for each region is interpolated and averaged.

Table 1 lists the ERBE data products being placed in the archive at the National Space Science Data Center (NSSDC). Product S-1 is the Raw Archival Tape (RAT). It contains the data from the telemetry stream, the converted housekeeping data, and the field-of-view (FOV) locations. Product S-5 is a plot of the satellite orbits on a single day, which can help locate observations for particular places. It is archived in the Monthly Product Summary for the S-1 Tapes. Product S-2 provides output from the ERBE solar monitors. Product S-8, the Processed Archival Tape (PAT), is the basic instantaneous form of data. It includes radiances and TOA fluxes. The inversion processing system produces this daily data tape. Products S-9 and S-10 contain monthly averaged scanner and nonscanner data, respectively. These monthly data tapes include the observations of each geographic region at the nearest hour. On S-9, for example, there are averages for each observed day and hour of the month. Finally, product S-4 is a single, monthly tape containing regional, zonal, and global spatial averages of the shortwave and longwave fields.

In the three sections that follow, we will discuss these areas in somewhat more detail. The first section provides information on the instrument data reduction and calibration. The second section deals with the inversion system. The third section describes some of the details of the averaging portion of the processing system.

Instrument Data Processing and Calibration. Both the scanner and the nonscanner are thermal instruments that convert radiation to heat. They use the resultant temperature variations to measure the radiation. In the scanner, the temperature change induces a change in the resistance of the thermistor flake. A bridge circuit measures the temperature change. In the nonscanner, the radiation substitutes for electrical heating of the cavity. The electrical power reduction is the measured quantity. For either detector type, the data reduction equations were derived by simplifying detailed mathematical models of the instrument heat flows.

The scanner observes space once every 4 seconds, which establishes a zero point for the measurement. Careful design minimizes the remaining sources of variability due to the instrument thermal environment. For example, the field stop which controls the shape of the optical portion of the PSF is gold plated on the back. This avoids transient radiative exchange with the detector flake. The data reduction algorithm for each scanner channel is linear in counts. A simple approximation is

$$\tilde{L}_i \approx G(m_i - m_{space} - O_i). \tag{1}$$

The actual algorithm is somewhat more complex. In this expression, $\tilde{L}_i$ is the filtered radiance at the i'th scan sample. m_i is the telemetry count for this sample. m_{space} is

the interpolated space count from the space observation before and after sample i. G is the gain; O_i is a set of offsets. Ground calibrations determine G, essentially the absorbed radiance per count. The offsets are an electronic artifact. For ERBS, observations of space provide their values. For NOAA-9 and NOAA-10, observations of the dark side of the earth determine the SW offsets. ERBS observations of the dark-side orbit crossings determine the TOT and LW offsets for the other two satellites.

The equations for nonscanner data reduction are more complex because the heat exchange between the cavity and its surroundings influences the detectors. These surroundings include a FOV limiter and, on the SW channels, a silica filter in the shape of a dome. Platinium Resistance Thermometers (PRT's) measure the temperature of the FOV limiters. For the total channels, the data reduction equation is

$$E_T \approx -A_V^T m^2 + A_F^T T_F + B^T. \tag{2}$$

This equation relates the measured counts, m, to the irradiance of the cavity, E_T. A_V^T is equivalent to a detector gain, and B^T to an offset. A_F^T is a coefficient to represent the energy exchange between the cavity and the FOV limiter, with its temperature T_F. For the SW channels, the equation includes the correction for the dome-to-cavity heat exchange. The equation for converting SW telemetry to instrument irradiance is

$$E_S \approx -A_V^S m^2 + A_E^S E_T + A_F^S T_F + B^S. \tag{3}$$

The superscripts on the coefficients distinguish the channels: S for SW, T for TOT. The numerical value of these coefficients varies, of course, from channel to channel.

Observations of known sources in a vacuum chamber on the ground provide the basic coefficients for these equations. In orbit, solar observations determine the values of A_V. Internal calibration sources or observations of the dark side of the earth determine the inflight values of B. The FOV limiter and filter dome corrections are quite important, although they are small (only a few $\mathrm{W\,m^{-2}}$). Ground calibration observations provide the basic values for the A_F and A_E coefficients.

Inversion Data Processing. The relationship between satellite-altitude radiance and TOA flux is

$$M = \frac{\pi L}{R}. \tag{4}$$

L is the radiance from a given point on TOA. M is the flux there. R is an Angular Distribution Model (ADM). In the longwave part of the spectrum, R is usually a limb-darkening model. In other words, R is less than 1 for radiances close to the horizon. R is usually greater than 1 for radiances going straight up. For reflected sunlight, the angular pattern depends on the height of the sun and on the azimuth of reflected sunlight. Thus, the SW R is a bidirectional reflectance model. Typically, R is close to 1 for all directions when the sun is overhead. However, when the sun is close to the horizon, R provides limb-brightening and strong azimuthal asymmetry. For both SW and LW, R depends on the underlying geography and on cloud conditions.

For the scanners, there are three parts to the inversion process. The first part is to identify the scene. The second is to remove the spectral coloration of the instruments. This also involves knowing the scene type since different scenes have different spectra. The third and final part is to compute the flux using equation (4).

For the WFOV and MFOV instruments, a Fredholm integral equation of the first kind relates the measured satellite irradiance, $\tilde{M}$, to the desired TOA flux, M. As an equation

$$\tilde{M} = \int d\theta \int d\phi K(\theta, \phi) M. \tag{5}$$

M is a function of position on TOA, while $\tilde{M}$ is a function of the satellite position. The kernel, K, of this expression depends upon three factors. The first is the satellite position. The second is the location of the TOA point. The third is the angular pattern of the TOA field. The satellite position and the TOA location specify the spherical polar coordinates θ and ϕ. These angles, together with the scene information, determine the appropriate value of R.

The processing system uses two inversion methods to retrieve M from nonscanner data. The simpler, known as the shape-factor technique, is similar in concept to Chahine's method of profile inversion [Chahine, 1970]. This method assumes that the data at satellite altitude come from a constant field of LW flux or of albedo. This assumption allows us to remove the flux from the integral. In symbolic terms,

$$\tilde{M} = \langle M \rangle \int d\theta \int d\phi K(\theta, \phi) = \langle M \rangle f. \tag{6}$$

f is the ***shape factor***. For the LW measurements from the WFOV instruments, f is constant and similar to a simple inverse square relationship,

$$f_{WFOV} = \left(\frac{\rho}{\rho + h} \right)^2. \tag{7}$$

ρ is the earth's radius, while h is the satellite altitude. The flux leaves the atmosphere from the subsatellite point, which provides an appropriate colatitude and longitude.

The more complex inversion technique is a numerical filter, e.g., [Twomey, 1965]. It is closer in philosophy to other methods of profile inversion, such as those described in Twomey's book [1977]. The paper by Smith et al. [1986] provides more complete details of the inversion procedures.

The data processing system produces the Processed Archival Tape (PAT) at the end of inversion processing. There is one PAT for each day of observation by a single satellite. Scientific work with the instantaneous scanner data should use the PAT's. These contain filtered radiances, scene identifications, unfiltered radiances, and TOA fluxes for each located pixel. The PAT's also have the satellite altitude irradiances and instantaneous TOA fluxes from the nonscanners. Table 2 provides a more detailed logical description. PAT data products have been archived at NSSDC starting in December 1987. They are available on magnetic tape, along with a detailed user's guide.

Averaging Data Processing. To complete the ERBE data processing, two subtasks remain: regional and time averaging. Geographic averaging is not conceptually difficult. However, the time averaging proceeds on a region-by-region basis. Thus, the data must be transformed from the time series of satellite observations into a regional data base. The size of the monthly data base makes this sorting a nontrivial operation.

The time interpolation process for a given geographic region involves a subtle interplay between the scene identification and the flux data. For the SW fluxes, time interpolation must consider that the albedo of a given scene type depends upon solar zenith. Quantitatively,

$$a(\mu_0(t)) = a(1)\delta(\mu_0(t)). \tag{8}$$

$\mu_0(t)$ is the cosine of the solar zenith angle at time t. Date, time of day, and latitude determine $\mu_0(t)$. $a(1)$ is the albedo at overhead sun. Like the ADM's, the directional models, $\delta(\mu_0)$, also depend upon the scene identification. Thus, once a scene type is available, so is this curve. From a flux observation with a given scene type, equation (8) provides the albedo for overhead sun. The daily average of reflection comes from applying this equation to other times of the day. For the LW fluxes, time interpolation must consider that desert and land surfaces respond to solar energy. They heat as they absorb sunlight and cool after the sun sets. Accordingly, the ERBE data processing system uses a model of daytime heating – provided the scene identification is clear [Brooks and Minnis, 1984]. Brooks et al. [1986] provide further details of time averaging.

At the end of time averaging, the data processing system produces three major archival products. The data products known as S-9 and S-10 contain the regionally ordered time history of observations for each region. The S-9 product comes from the time series obtained from each scanner. Figure 1 shows the arrangement of data for a given month in each geographic region. Table 3 gives the logical structure of the S-9 product. This product is moderately voluminous, with four to five tapes per month. The S-10 product is similar to the S-9 in format, but it contains data only from the nonscanners. The S-10 contains TOA fluxes inverted using both the shape factor and the numerical filter methods. Product S-10 has a volume of four tapes per month. The S-4 product is a regional and zonal monthly average for combined satellite data. This data product is further described in Table 4. It has a volume of one tape per month.

This is an overview of the ERBE data processing and its major archived data products. The Science Team has anticipated a large interest in the monthly averaged

products. Accordingly, in producing these products, they have tried to balance the need for data compression against the need for detailed process understanding. In the following section, we will describe the major features of the validation process for these products. Then we will provide a summary of the contents of the monthly averaged data products for the first archived month.

An Overview of ERBE Validation

It may seem strange that measurement of radiation budget requires a massive data processing system. For example, ERBE's system uses about 250,000 lines of FORTRAN code. This system also uses an additional 150,000 lines for offline diagnostic work. However, because of the stringent requirements for accuracy in the budget, details are important.

Table 5 shows the number of parameters used by various parts of the data processing system. The coefficients in this table are conveniently arranged in three groups. The first group is the set of "calibration coefficients" that appear in the algorithms converting telemetry counts to instrument irradiation. Ground and inflight calibration sources provided these coefficients. The second group includes the ADM's and spectral unfiltering coefficients needed for inversion. A categorization of the Nimbus 7 ERB measurements [Taylor and Stowe, 1984] forms the base for the ADM's. Missing bins were filled using the reciprocity principle [Suttles et al., 1988; Suttles et al., 1989]. A combination of radiative transfer results and measurements of the instrument spectral responses [Avis et al., 1984] provides the spectral correction coefficients. The third and final group of parameters consists of the coefficients needed for time averaging, mainly the directional models. These

also came from the Nimbus 7 ERB, but have been suitably supplemented by GOES observations where needed. Table 5 clearly shows that the bulk of the coefficients come from the inversion process.

The earth's radiation budget is not easy to measure, even indirectly. In a utopian measurement scheme, cavity radiometers on 10,368 tethered balloons would determine the TOA fluxes. These would fly over each 2.5° geographic region of the earth at the height of the top of the atmosphere. They would have to be in enough of a vacuum to avoid convection within the instruments. Since such an in situ measurement is impractical, the Science Team has relied on consistency and measurement intercomparisons for validation. Fortunately, ERBE data provide a number of these checks. The Science Team chose 10 of these as validation criteria. These criteria provide a way of judging the consistency of the various parameters in the data processing system. In the material that follows, we discuss each of them briefly.

Table 6 provides a brief summary of how the Team divided its efforts on these criteria. Table 7 summarizes the influence of the various parameters upon each criterion. Aside from the first criterion (an independent check of each channel's calibration), none of these criteria tests only a single parameter. The further along in the processing system we look, the more parameters there are that can affect the results. Table 8 provides a synopsis of the results of examining each of these criteria.

Consistency of Independent Checks of Sensor Calibration

Preflight ground calibration is the basis for ties between the ERBE data and fundamental physical units. The detailed mathematical models of the detector physics provide

the form of the equations for count conversion. Observations of known sources with variable instrument environments provide the data for a statistical determination of coefficients. For the total (and scanner LW) channels, a variable-temperature blackbody provided data to determine gains and nonscanner heat exchange coefficients. An integrating sphere observed by both the SW and total channels provided data to determine the coefficients for the SW channels. The total channels determined the sphere's output. Silicon photodiodes monitored the source stability between SW and total channel observations. The ERBE instruments observed all of these the calibration sources in a vacuum chamber to avoid unmodeled convective heat exchange.

In orbit, the ERBE instruments can check the ground calibrations in several different ways. First, all of the instruments can use the sun as a calibration source. The nonscanners observe the sun through a solar port. The scanners can observe it reflected from an attenuator plate. Second, the instruments can observe deep space through the solar port on the nonscanners and during each scan on the scanners. On ERBS, the satellite also pitched over twice to observe space and the sun throughout an entire orbit. Third, each instrument package carries a set of internal calibration sources. There are blackbodies for the total (and scanner LW) channels. For the SW channels, there are tungsten lamps.

The nonscanner solar observations have detected, quantified, and corrected for a transmission loss (about 1/4% per month) in the WFOV SW filters. Solar ultraviolet exposure caused this loss. The solar observations also set the inflight gain of the nonscanner channels. Two months into the flight, ground controllers turned the ERBS onto its back so that the instruments faced space instead of the earth. This maneuver provided observations to determine scanner offsets for earth observations. A second pitchover about 1 year later

confirmed these values. We have not used the internal calibration data to adjust the count conversion coefficients, except for the B term on the NOAA-9 nonscanners. In this case, we adjust B^T and B^S to agree with the calibration observations.

Overall, the internal calibration sources have served as monitors of stability and precision. Figure 2 provides a sample of data from the internal calibration observations of the ERBS scanner [Lee et al., 1987]. This figure shows the changes that would be required to bring internal calibration observations into agreement with the sources. For all three channels, the apparent changes are less than 0.5% over the 3 years of observations. At this level, no adjustments appear justifiable and none have been made.

The only parameters affecting the independent calibration interpretations are the instrument coefficients (summarized as a gain and an offset for each instrument type). Table 7 reflects this dependence. The entry in Table 8 for criterion 1 summarizes the overall level of agreement for this criterion. This criterion does not deal with the relative intercomparison of the calibration sources on the scanner and nonscanner. However, we can say that the instruments are radiometrically stable.

Satellite Altitude Agreement of Scanner and Nonscanner

During the normal ERBE observations, each crosstrack scan observes from one side of the orbital track to the other. The scan extends from limb to limb. In addition, each scan overlaps the one before and the one after. Thus, the scanners observe the same geography as the nonscanners, although not quite from the same direction. The scanner sees a particular point on the earth only perpendicular to the satellite ground track. The nonscanner sees it more obliquely at an earlier or a later time. Thus, the

scanner measurements can be "turned" to the nonscanner directions with the ADM's and integrated over the nonscanner field of view. This integrated value provides a simultaneous, colocated scanner simulation of the nonscanner measurement at satellite altitude.

Figure 3 shows one such intercomparison for SW observations by the scanner and by the WFOV on ERBS on April 13, 1985. Several Science Team members have used similar scatter plots to assess the performance of the two types of instruments. This intercomparison criterion is not as simple to interpret as the calibration checks of criterion 1 because the satellite altitude intercomparison requires ADM's. However, both analytical and numerical studies show that the satellite-altitude intercomparisons are much more sensitive to instrument coefficients than to the ADM's. The entries in Table 7 reflect this dependence. For the example shown in Figure 3, the mean difference between the two data types is $-2.1\,\mathrm{W\,m^{-2}}$. The standard deviation of the intercomparison is $4.0\,\mathrm{W\,m^{-2}}$. Since the mean SW flux on the instrument is $205\,\mathrm{W\,m^{-2}}$, these data agree to within $1 \pm 2\%$. The LW agreements are similar, with an even smaller standard deviation. Table 8's entry for criterion 2 summarizes the experience with the satellite altitude intercomparison.

Agreement of Instantaneous, Colocated Measurements on Several Satellites

There are many opportunities each month for nearly simultaneous observations of the areas near the orbit intersection between two of the ERBE satellites. Figure 4 shows an example of such an intercomparison of the SW fluxes for the ERBS and NOAA-9 scanners. Each data point comes from the nine $2.5° \times 2.5°$ geographic regions that surround an orbit intersection. In addition, each NOAA-9 regional average is for data obtained within 10 minutes of the ERBS overpass. The slope of the regression line in Figure 4 is 1 ± 0.01,

showing that the two scanners are on the same radiometric scale. The mean bias of the intercomparisons is less than $2\,\mathrm{W\,m^{-2}}$, and the standard deviation is $15\,\mathrm{W\,m^{-2}}$. In the longwave, the results are similar, except that the standard deviation is about $5\,\mathrm{W\,m^{-2}}$.

The instrument parameters and the ADM's both enter this type of intercomparison, as suggested in Table 7. The excellent agreement of the slopes of the regression curves suggests that the instrument calibrations are on the same scale.

Spectral Consistency of Three Channel Scanner Observations from a Single Satellite

Because the three scanner telescopes are bore-sighted, their fields of view overlap more than than 98 %. Thus, the spectral overlap of the three channels provides a redundant measurement of the SW and LW radiances. This redundancy can assess the uncertainty arising from the spectral coloration of these instruments. In other words, the discrepancy

$$\delta_{spectrum} \equiv C_{TOT}\tilde{L}_{TOT} - C_{SW}\tilde{L}_{SW} - C_{LW}\tilde{L}_{LW} \tag{9}$$

gives a quantitative indication of the level of disagreement. The coefficients C are derived from the correction matrices used for production of broadband LW and SW [Avis et al., 1984]. Three factors determine the correction matrices. The first is the scanner channels' measured spectral sensitivity. The second is radiative transfer computations of the radiance spectral distribution. The third is a model of the statistical distribution of earth scenes. Figure 5 shows one example of a histogram of $\delta_{spectrum}$ for clear ocean observations on April 20, 1985, by ERBS.

Table 7 shows that this intercomparison exercises our understanding of both the scanner calibration and the spectral distribution of the earth radiances. ADM's do not

influence this intercomparison because it uses the radiances directly. Table 8's entry for this criterion summarizes the results from many intercomparisons. For ERBS, the mean deviation is less than $1\,W\,m^{-2}\,sr^{-1}$. Standard deviations of the histograms are 1 to $2\,W\,m^{-2}\,sr^{-1}$. For NOAA-9, the mean discrepancy is also less than $1\,W\,m^{-2}\,sr^{-1}$ at night, and about $2\,W\,m^{-2}\,sr^{-1}$ during the day.

Instantaneous Top-of-the-Atmosphere Agreement of Scanner and Nonscanner

We can also compare the scanner and nonscanner fluxes at TOA. We must integrate the inverted scanner fluxes over a geographic region comparable to the effective resolution of the nonscanners. This is typically a circular area with a diameter of about 4° for the MFOV and 7° for the WFOV. In this case, the ADM's have a stronger influence on the result, particularly for the MFOV. Table 7 reflects that influence.

Figure 6 shows a scatter diagram between SW scanner fluxes and a shape-factor inversion of SW WFOV measurements. The SW fluxes are more difficult to reproduce than the LW fluxes because the SW angular pattern is more variable. The mean difference in Figure 6 is $0.6\,W\,m^{-2}$, with a standard deviation of about $23\,W\,m^{-2}$. Since the mean flux for these data is about $220\,W\,m^{-2}$, the relative agreement is $0.3 \pm 10\%$. Table 8's entry for this criterion summarizes this experience for both the SW and LW intercomparisons. Again, the instruments are on the same radiometric scale. Furthermore, the ADM's do not produce global biases in this intercomparison.

Satisfactory Checks of Limb Darkening and Bidirectional Models

The Angular Distribution Models are fundamental to the ERBE data processing. Accordingly, the Science Team checked them four ways. First, Brooks and Smith used observations taken with scans along the orbit track. These look at a particular target from many different directions. Second, Coakley and his coinvestigators placed the ERBE data in angular bins to produce ERBE angular models. Third, Suttles and Wielicki inverted the Nimbus 7 ERB scanner observations with the ERBE Maximum Likelihood Estimator (or MLE: [Wielicki and Green, 1989]) and with Arking and Vemury's [1984] Sorting into Angular Bins approach. This produces two statistically averaged "fluxes" for comparison (although these are not same as time averaged fluxes). Fourth, Green, Wielicki, and Davies averaged the ERBE scanner observations as a function of viewing zenith.

The first method of independently checking the ADM's is to use alongtrack data. These are available from observations in January and August of 1985 [Brooks and Fenn, 1988; Smith et al., 1988]. In this mode of operation, the scanner sees a pixel along the ground track from several different directions. All of the observations lie in the plane formed by the satellite trajectory as it passes through the local zenith. The scene type should remain fixed during the 15 minutes required for a single overpass. Thus, the only variations are those from the scene angular dependence and the possible misidentifications of the ERBE scene categories.

Figure 7 shows normalized radiances identified as partly cloudy from near-nadir ERBS observations. First, we divided the observed radiance by the nadir radiance. Second, we divided the quotient by the ADM for that scene. The resulting number would be 1.0 if the model were perfect. As Figure 7 shows, the model is less limb-darkened than it

needs to be by about 2%. The only significant deviation is for partly cloudy scenes over coastal regions. This deviation is not important globally since such regions cover only a few percent of the total area of the earth. The opposite holds true in the SW, where the earth appears slightly more limb-brightened than the operational ADM's. The incorrect angular modeling is somewhat mitigated by having areas with too high a flux partially balanced by areas with too small a flux.

The second approach to checking the ERBE ADM's is develop models based on ERBE data alone. This approach begins by placing the ERBE scanner data into angular bins. Then, the binned data are integrated to produce a flux. Finally, the radiances are divided by the flux to produce ADM's. The new models are then compared with the original ADM's. The comparison suggests that the ERBE models are unbiased overall. However, there are some models in which the ERBE ADM's are significantly different from the ADM's in the data reduction software.

A third approach to checking the ERBE MLE/ADM procedure has been to use a different "inversion" algorithm on a month of Nimbus 7 ERB scanner data. The alternative method is the Sorting into Angular Bins approach of Arking and Vemury [1984]. Table 9 shows the results from this investigation [Vemury, 1987]. The monthly averaged albedo and longwave flux differ by very small amounts on a global basis.

Finally, averages of the scanner data as a function of scan sample number (or, equivalently, viewing zenith) can check the ADM's. The results of this procedure are consistent with those found by the alongtrack investigation.

As noted in Table 7, the ADM's are the primary influence on these intercomparisons. There is little influence from the other parameters in the processing system. The

ERBE Science Team feels that the errors found in these investigations are not large enough to force further revisions to the ADM's for operational ERBE data processing.

Satisfactory Checks of Scene Identification

The major check of the ERBE scene identification has come through the use of a special validation data set containing ERBE, AVHRR, and HIRS data. Three separate groups on the ERBE Science Team have used this product with their own cloud retrieval algorithms. Each produced estimates of the proper scene identification for the ERBE pixels on this product.

The first of these investigations [Diekmann and Smith, 1989] used radiative transfer calculations to determine the expected radiances for clear and cloudy scenes. These radiances were then used in a MLE method for the AVHRR radiances to identify the proper scene for the ERBE pixels. The intercomparison can be conveniently summarized in the form of a four category misclassification matrix, similar to that shown in Table 10. To produce this Table, the theoretical MLE for AVHRR data classifies each ERBE pixel into the four ERBE cloud categories. The result is an AVHRR classification and an ERBE classification. Each pair of classifications provides a sample which is added to a histogram of results. Thus, Table 10 summarizes the statistical distribution of ERBE/AVHRR-theoretical MLE classifications. Diekmann and Smith found that ERBE classified 2/3 of the pixels correctly, while most of the remainder were misclassified by one scene type. The misclassification matrix can then provide an estimate of the flux error caused by the scene identification error. Diekmann and Smith's intercomparison over the midlatitude eastern Pacific suggests that the errors are 2-5 $W\,m^{-2}$ in the LW and 2-7 $W\,m^{-2}$ in the SW.

Minnis et al. [1986] examined the same data set with the Hybrid Bispectral Thresholding Method (HBTM). Coakley and collaborators examined this set with the Spatial Coherence (SC) method [Coakley and Bretherton, 1982, 1983; Coakley and Baldwin, 1984]. Both alternative classification schemes have results that are similar to those of Diekmann and Smith – ERBE has correctly identified over 2/3 of the pixels. However, the HBTM and SC intercomparisons are not necessarily consistent with each other or with the theoretical MLE method.

More work remains in this validation area. The primary purposes of the scene identification are choosing the proper ADM for inversion and improving the time averaging interpolation. The Science Team has concluded that the scene identification does not introduce significant overall errors in the final ERBE data products. More detailed understanding of the MLE classification will follow as the Team members complete their detailed investigations.

Satisfactory Checks of Time Averaging

Even with three satellites, ERBE does not sample all hours of the month. Accordingly, ERBE has adopted a moderately sophisticated method of interpolating across the missing hours [Brooks et al., 1986]. Part of the work of validation has involved simply checking that this time interpolation is working correctly. A more detailed assessment requires some form of correlative information. Over the western hemisphere, the Geostationary Operational Environmental Satellite (GOES) has supplied improved time sampling. Over Europe and the Sahara, Meteosat has supplied it.

Figure 8 shows an example of such a validation time series, with ERBE shown by the solid line and GOES by the crosses. ERBE does not measure fluxes at the missing times. GOES is a narrow spectral band instrument which observes a particular spot on the earth from a fixed direction. Thus, each source of information has its own peculiar sources of uncertainty.

In general, the results of this detailed investigation are consistent with those published earlier [Harrison et al., 1983; Brooks and Minnis, 1984]. The time interpolation and averaging of regional ERBE data introduce uncertainties in the regional monthly averages less than 1.5 $W\,m^{-2}$ for LW and less than 5 $W\,m^{-2}$ for SW.

Checks Against Other Sources of Data

Although ERBE contains many internal consistency checks, it is important to compare ERBE data with other radiation data. There have been three major types of comparison. First, ERBE scanner radiances have been compared with radiative transfer computations of radiance. Second, ERBE data have been compared with the Nimbus 7 ERB observations. Third, ERBE averages have been compared with averages of Outgoing Longwave Radiation (OLR) from other instruments.

The ERBE scanners are a source of absolutely calibrated radiances. Therefore, their data are directly comparable with computed radiances for carefully chosen targets. The most fruitful comparisons come from clear, nighttime observations of sites with nearly simultaneous radiosonde observations. Ramanathan and Downey [1986] report one example of such work. They carefully edited 50,000 soundings for clouds, radiance homogeneity, and sounding errors. This produced about 50 intercomparison possibilities. The ERBS

LW scanner radiances agreed with the computations to within about 1%. Ramanathan and Briegleb [1986] compared ERBE observations with clear-sky albedos, obtaining similar results. This level of agreement provides confidence in both the scanner and the transfer computations.

At larger space and longer time scales, ERBE data and Nimbus 7 ERB WFOV measurements have been compared. With suitable adjustments, the Nimbus 7 data may provide a long-term precursor to the ERBE data for coarse resolution measurements of fluxes.

ERBE instantaneous and monthly fluxes have also been compared with AVHRR LW estimates. Although the agreement is reasonable, there are differences in detail, particularly for high and low values of the OLR. There, the regression curve differs from the ERBE observations.

As we suggest in Table 7, the intercomparisons between ERBE and other types of data do not identify a specific major parameter for investigation. Rather, they provide information regarding potential problems whose detailed dependencies must be resolved using other types of intercomparisons. The results of these intercomparisons between ERBE and other data suggest no major discrepancies in the ERBE data.

Reasonableness of Global, Annual Net Radiation

The final ERBE validation criterion has been the reasonableness of the global, annual-averaged radiation balance. Because the detailed intercomparisons described in the last few pages are very costly of man and machine time, the Team selected 4 months with both ERBS and NOAA-9 data for validation. These months are April, July, and

October of 1985, and January of 1986. Their even spacing over the year should give a resonable estimate of the annual average fluxes. Based on these 4 months, the ERBE global, annual average albedo is 0.299, and the emitted flux is 235 $W\,m^{-2}$. The annual average net radiation balance is 6.1 $W\,m^{-2}$. This is about the uncertainty obtained by some preliminary estimates.

A Summary of the Results of ERBE Validation

During the early phases of the validation effort, the Science Team adopted a strategy to balance the need for detailed examination with the need for stability. Detailed examination requires intensive processing of small amounts of data on a few days. Testing stability of the system requires routine processing of long series of data with the same coefficients. The 4 months we have already mentioned seem to strike the right balance. Within each of these 4 months, detailed investigations used 4 "validation days" about 5 days apart.

As a result of this strategy, the ERBE data will not enter the archive in a continuous time sequence. The 4 validation months will enter it first. At the time of this writing, the ERBE Science Team has placed the following priority on the sequence for data archival:

1. 4 validation months: April, July, and October 1985; January 1986
2. ERBS month: November 1984
3. Alongtrack months: January and August 1985
4. FIRE validation month: October 1986
5. NOAA-10 month: December 1986
6. Completion of 1 year: April 1985 - March 1986

It may be useful to summarize preliminary estimates of uncertainties in various products. The following numbers represent estimates of the standard deviations about a given data point within which the true measurement might lie. They are not definitive confidence intervals, but are intuitively based on the observed discrepancies in the intercomparisons. It is also important to remember that different measurements have different uncertainties. First, for instantaneous radiances, we expect uncertainties of about 1% for longwave observations of filtered radiance and 2-3% for shortwave. Radiative transfer comparisons (criterion 9) and spectral consistency (criterion 4) provide the basis for this uncertainty estimate. Second, on an instantaneous observation of flux from 2.5°× 2.5° geographic regions, the ERBS/NOAA-9 intercomparisons shown in Figure 4 offer reasonable estimates of uncertainty (criterion 2). These are $\pm 5\,\mathrm{W\,m^{-2}}$ in the longwave and $\pm 15\,\mathrm{W\,m^{-2}}$ in the shortwave. Third, on a monthly average, regional basis, the uncertainties in the scanner data are about $\pm 5\,\mathrm{W\,m^{-2}}$ for SW and $\pm 5\,\mathrm{W\,m^{-2}}$ for LW. These come from simulations with GOES data. This uncertainty represents no change from the preflight estimate published by Brooks et al. [1986]. The nonscanner averages may be somewhat more uncertain because of sampling and the diurnal averaging process. Fourth, the uncertainty in global, annual average net radiation is probably about $\pm 5\,\mathrm{W\,m^{-2}}$. This estimate is based on the imbalance obtained using scanner data from the 4 validation months (criterion 10). A definitive error analysis is being actively pursued. However, it requires a number of developments in measuring the covariances of the radiation field. It also requires developments for handling uncertainty estimation in the presence of irregular and sparse time, space, and angle sampling.

ERBE Data for January 1986

An article by the ERBE Science Team [1986] presented PAT data for November 1984. Readers that want to sample that type of data should consider the figures in that paper. In this section of the paper, we will show more of information from the monthly type of archival data.

Figure 9 shows the monthly average reflected radiation field for January 1986. In this month, the sun hovers near 20° south declination. As a result, the solar irradiance of the earth has a broad maximum near 20° S. The monthly average reflected flux mirrors this incident power density. It is interesting to see the cloud fields centered over the Amazon, the Congo, and the Indonesian "water continent." These reflect the January position of a portion of the Intertropical Convergence Zone and the corresponding fields of heavy convective activity. We can also see the low stratus decks off the western coast of South America and the western coast of Africa. The most notable feature is the very large reflection from the Antarctic ice sheet. There, the combination of high irradiance and high albedo produce the highest average reflection of any location on earth.

Figure 10 shows the monthly average longwave field for the same month. The Sahara also stands out in this picture, as does the northern Indian Ocean. These areas are quite warm, reflecting both the high surface temperature and the lack of humidity in the overlying atmosphere. The deep convective storms over the Amazon, the Congo, and Indonesia are also quite visible. However, the low stratus decks off the western coasts have almost entirely disappeared. The temperature contrast between the cloud tops and the clear oceans in these regions is low. In the broadband radiation field, this contrast is further obscured by the similarity of the cloud and water vapor distributions.

Figure 11 shows the net radiation during January 1986. In contrast to the two previous maps, this figure shows a very strongly zonal picture. It almost seems that the earth-atmosphere system abhors longitudinal structure. This suggests that the atmospheric circulation wipes out almost any longitudinal variations in net radiation. The Sahara persists as an anomaly to this picture, as Charney [1975] noted some time ago. While most of the latitude zone near 20 °N has a negative net radiation, the Sahara and the atmosphere above it have a strongly negative energy balance. Thus, we might expect the rest of the latitude belt to have to supply this energy.

For this month, the earth's albedo was 0.309, while the longwave flux was 232 W m^{-2}. Thus, the ERBE measurements give a net balance of about 13 W m^{-2} for January 1986.

ERBE Data Availability

The ERBE data will be available to the scientific community through the National Space Science Data Center. For requesters within the United States, the address is

NATIONAL SPACE SCIENCE DATA CENTER

CODE 633.4

GODDARD SPACE FLIGHT CENTER

GREENBELT, MARYLAND 20771

For scientists outside the United States, the address is

WORLD DATA CENTER A

ROCKETS AND SATELLITES

CODE 630.2

GODDARD SPACE FLIGHT CENTER

GREENBELT, MARYLAND 20771, USA.

The ERBE data will begin to flow into the NSSDC archive on a reasonably regular basis in the near future. The Science Team has agreed to freeze the data processing system. The only changes are in the count conversion coefficients (such as the continuing changes in WFOV SW dome transmissions) and the snow maps. As we have tried to make clear throughout this paper, the validation effort represents a large cooperative effort involving the ERBE Science and Data Management Teams. The investigators listed in Table 6 should publish detailed reports on their work on the validation criteria in the near future.

The Science Team may consider improvements to various aspects of the data processing in the future. However, the Team recognizes the importance of these data for the scientific community and will probably be reluctant to make large changes. This data set should make a major contribution to our understanding of the current state of the earth's climate system.

References

Arking, A. and S. Vemury, The NIMBUS 7 ERB data set, a critical analysis, *J. Geophys. Res.*, **89**, 5089-5097, 1984.

Avis, L. M., Richard N. Green, John T. Suttles, and Shashi K. Gupta, A robust pseudo-inverse spectral filter applied to the Earth Radiation Budget Experiment (ERBE) scanning channels, *NASA Technical Memorandum 85781*, NASA Langley Research Center, Hampton, VA, 1984.

Barkstrom, B. R., The Earth Radiation Budget Experiment (ERBE), *Bull. Amer. Meteor. Soc.*, **65**, 1170-1185, 1984.

Barkstrom, B. R. and G. L. Smith, The Earth Radiation Budget Experiment: science and implementation, *J. Geophys. Res.*, **24**, 379-390, 1986.

Brooks, D. R. and M. A. Fenn, Summary of along-track data from the Earth Radiation Budget Satellite for several major desert regions, *NASA RP 1184*, NASA Langley Research Center, Hampton, VA, 1988.

Brooks, D. R. and P. Minnis, Simulation of the earth's monthly average regional radiation balance derived from satellite measurements, *J. Climate Appl. Meteor.*, **23**, 392-403, 1984.

Brooks, D. R., E. F. Harrison, P. Minnis, J. T. Suttles, and R. S. Kandel, Development of algorithms for understanding the temporal and spatial variability of the earth's radiation balance, *Rev. Geophys.*, **24**, 422-438, 1986.

Chahine, M. T., Inverse problems in radiative transfer: determination of atmospheric parameters, *J. Atmos. Sci.*, **27**, 960-967, 1970.

Charney, Dynamics of deserts and drought in the Sahel, *Quart. J. Roy. Meteo. Soc.*, **101**, 193-202, 1975.

Coakley, J. A. Jr. and D. G. Baldwin, Towards the objective analysis of clouds from satellite imagery data, *J. Climate and Appl. Meteor.*, **23**, 1065-1099, 1984.

Coakley, J. A. Jr. and F. P. Bretherton, Cloud cover from high-resolution scanner data: Detecting and allowing for partially filled fields of view, *J. Geophys. Res.*, **87**, 4917-4932, 1982.

Coakley, J. A. Jr. and F. P. Bretherton, Properties of multi-layered cloud systems from satellite imagery, *J. Geophys. Res.*, **88**, 10818-10828, 1983.

Diekmann, F. J. and G. L. Smith, Investigation of scene identification algorithms for radiation budget measurements. *J. Geophys. Res.*, in press, 1989.

ERBE Science Team, First data from the Earth Radiation Budget Experiment (ERBE), *Bull. Amer. Meteor. Soc.*, **67**, 818-824, 1986.

Harrison, E. F., P. Minnis and G. G. Gibson, Orbital and cloud cover sampling analyses for multisatellite earth radiation budget experiments, *J. Spacecraft and Rockets*, **20**, 491-495, 1983.

Huck, F. O., N. Halyo, and S. K. Park, Information efficiency of line-scan imaging mechanism, *Appl. Opt.*, **20**, 1990-2007, 1981.

Kopia, L. P., The Earth Radiation Budget Experiment scanner instrument, *Rev. Geophys.*, **24**, 400-406, 1986.

Lee, R. B. III, B. R. Barkstrom, S. M. Natarajan, M. A. Gibson, N. Halyo, and D. A. Chrisman, Broadband calibration of the NOAA 9 Earth Radiation Budget Experiment (ERBE) scanning radiometers, *EOS*, **68**, 1217, 1987.

Luther, M. R., J. E. Cooper and G. R. Taylor, The Earth Radiation Budget Experiment nonscanner instrument, *Rev. Geophys.*, **24**, 391-399, 1986.

Minnis, P., E. F. Harrison, and G. G. Gibson, Cloud cover over the equatorial eastern Pacific derived from ISCCP data using a hybrid bispectral threshold technique, *J. Geophys. Res.*, **92**, 4051-4073, 1986.

Ramanathan, V. and B. P. Briegleb, Comparison of ERBE inferred and model computed clear-sky albedos, *Proc. Sixth Conf. on Atmos. Rad.*, J32-J33, 1986.

Ramanathan, V. and P. Downey, An approach for verifying clear-sky radiation models with ERBS scanner measurements, *Proc. Sixth Conf. on Atmos. Rad.*, J28-J31, 1986.

Smith, G. L., R. N. Green, E. Raschke, L. M. Avis, J. T. Suttles, B. A. Wielicki, R. Davies, Inversion methods for satellite studies of the earth's radiation budget: development of algorithms for the ERBE mission, *Rev. Geophys.*, **24**, 407-421, 1986.

Smith, G. L., J. T. Suttles and N. Manalo, The ERBE alongtrack experiment, *Proc. International Radiation Symposium 1988*, 1988.

Suttles, J. T., R. N. Green, P. Minnis, G. L. Smith, W. F. Staylor, B. A. Wielicki, I. J. Walker, D. F. Young, V. R. Taylor, and L. L. Stowe, Angular radiation models for the earth-atmosphere system. Volume I: shortwave radiation, *NASA Reference Publication 1184*, NASA Langley Research Center, Hampton, VA, 1988.

Suttles, J. T., R. N. Green, G. L. Smith, B. A. Wielicki, I. J. Walker, V. R. Taylor, and L. L. Stowe, Angular radiation models for the earth-atmosphere system. Volume II: longwave radiation, *NASA Reference Publication 1184*, NASA Langley Research Center, Hampton, VA, 1989.

Taylor, V. R. and L. L. Stowe, Reflectance characteristics of uniform earth and cloud surfaces derived from Nimbus 7 ERB, *J. Geophys. Res.*, **89(D4)**, 4987-4996, 1984.

Twomey, S., The application of numerical filtering to the solution of integral equations encountered in indirect sensing measurements, *J. Franklin Institute*, **269**, 95-109, 1965.

Twomey, S., *Introduction to the Mathematics of Inversion in Remote Sensing and Indirect Measurement*, Elsevier Scientific Publishing Co., New York, 1977.

Vemury, S. K., Evaluation of the ERBE Scene Identification Algorithm, *NASA Contractor Report 178243*, NASA Langley Research Center, Hampton, VA, 1987.

Wielicki, B. A. and R. N. Green, Cloud identification for ERBE radiative flux retrieval, submitted to *J. Appl. Meteor.*, 1989.

Willson, R. C., Active Cavity Radiometer Type IV, *Appl. Opt.*, **18**, 179-185, 1979.

TABLE 1. ERBE ARCHIVAL DATA PRODUCTS

Designation	Contents	Medium	Period
	Telemetry Archival Products		
S-1	Raw radiometric counts, converted housekeeping, earth located (RAT)	Tape	Daily
S-5	Orbital ground track plots (archived in S-1 Monthly Product Summary)	Paper	Daily
	Products with Instantaneous Geophysical Observations		
S-2	Solar irradiance from bi-weekly calibrations	Tape	Monthly
S-8	Instantaneous scanner and nonscanner measurements inverted to the top of the atmosphere (PAT)	Tape	Daily
S-7	Instantaneous nonscanner measurements inverted to the top of the atmosphere	Tape	Monthly
	Products with Instantaneous, Regional Averages		
S-9	Regionally averaged scanner data	Tape	Monthly
S-10	Regionally averaged nonscanner data	Tape	Monthly
	Products with Monthly Averages Only		
S-4	Regional, zonal, and global averages of longwave, shortwave, and albedo at 2.5 ° and larger scales	Tape	Monthly

TABLE 2. ERBE PROCESSED ARCHIVAL TAPE (S-8) STRUCTURE

Organized into 16-second records (5400 records/day)

Each 16-second record has
- 4 earth scans, each with 62 earth observations per channel
- 20 nonscanner irradiances per channel

Data included in each record are
- Julian Date at record start
- Satellite position and velocity
- Scanner data for each earth sample
  - FOV position (colatitude and longitude)
  - Filtered radiances (TOT, SW, LW)
  - Unfiltered radiances (SW, LW)
  - Scene ID (1 of 12 geotype/cloud categories)
  - TOA fluxes (SW, LW)
- Nonscanner data for each sample
  - FOV position (colatitude and longitude)
  - Channel irradiance (TOT, SW)
  - TOA fluxes (SW, LW)
- Quality control flags

TABLE 3. ERBE MONTHLY ARCHIVAL TAPE (S-9 and S-10) STRUCTURE
[S-9 contains scanner data; S-10 contains nonscanner data]

Organized by geographic regions

Each region has 2 records:
- First record has monthly average values (fixed length)
- Second record has areal averages for observed hours and days (variable length)

Data for each monthly average (first record)
- Reflected flux
- Emitted flux
- Statistics (max, min, std. dev.)

Data for each observed hour box (second record)
- Reflected flux
- Emitted flux
- Statistics (max, min, std. dev.)
- Scene ID related information (scanner only)

TABLE 4. ERBE SPATIAL AVERAGING MONTHLY ARCHIVAL TAPE (S-4) STRUCTURE

Organized by geographic regions

Each region has 1 record with monthly average values

Monthly Grand Daily Average
- Reflected flux
- Emitted flux
- Clear-sky fluxes

Monthly Grand Hourly Average
- Reflected flux
- Emitted flux
- Clear-sky fluxes

Daily Averaged Flux – by day (31 values)
- Reflected flux
- Emitted flux
- Clear-sky fluxes

Hourly Averaged Flux – by hour (24 values)
- Reflected flux
- Emitted flux
- Clear-sky fluxes

Regional, Zonal and Global averages

Scanner (Regional: 2.5°, 5.0°, 10.0°; Zonal, Global)
MFOV Numerical Filter (Regional: 5.0°, 10.0°; Zonal , Global)
MFOV Shape Factor (Regional: 10.0°; Zonal, Global)
WFOV Numerical Filter (Regional: 5.0°, 10.0°; Zonal , Global)
WFOV Shape Factor (Regional: 10.0°; Zonal , Global)

TABLE 5. DATA PROCESSING PARAMETERS

Instrument Related Coefficients
Nonscanner Coefficients
4 coefficients for TOTAL channels
5 coefficients for SW channels
Scanner Coefficients
3 gain related coefficients for each channel
74 offsets for each channel
Scanner Point Spread Function
1 time delay for earth location
Matrix of numbers for sensitivity in instantaneous intercomparisons
Housekeeping Coefficients
5 temperature housekeeping coefficients for each PRT, including
3 PRTs for each nonscanner channel,
1 PRT for each scanner and 4 for internal calibration sources

Inversion Related Coefficients
Spectral Correction Spectra for Scanner
27840 SW radiance spectra
(72 wavelengths each, for 4 viewing zeniths, 5 viewing azimuths,
8 scene types, 3 latitude zones, and 12 months)
2112 LW radiance spectra
(45 wavelength bands each, for 4 viewing zeniths, clear and cloudy scenes,
day and night, 3 latitude zones, and 12 months)
Statistical Model of earth Scenes
Scanner Spectral Responsivities
One for each of 248 wavelengths for each scanner channel
Scanner Spectral Correction Matrices
19328 matrix elements, computed from scanner spectral responsivities and
spectral correction spectra

TABLE 5. DATA PROCESSING PARAMETERS (CONCL'D.)

Inversion Related Coefficients (Concl'd.)
Angular Models
3360 radiances and 3360 standard deviations used in scene identification and inversion for LW fluxes
6720 radiances and 6720 standard deviations used in scene identification and inversion for SW fluxes
Clear Sky Radiance Models
10368 clear-sky, overhead sun, regional albedos
120 scene albedos
Snow coverage database for each month

Averaging Related Coefficients
278 solar zenith angle models of albedo variation
10 longwave diurnal amplitudes

TABLE 6. VALIDATION CRITERIA AND RESPONSIBLE INDIVIDUALS

Criterion 1. Consistency of Independent Checks of Sensor Calibration

Deep Space Observations	Barkstrom Halyo Lee
Solar Observations	Lee Halyo
Flight Calibrations - Blackbodies	Barkstrom Lee Halyo
Flight Calibrations - Tungsten Filament Lamps	Lee Halyo Barkstrom
Shortwave Observations of Dark earth	Avis

Criterion 2. Satellite Altitude Agreement of Scanner and Nonscanner on Each Satellite

Simulate nonscanner data along the orbit	Green House Wu & Ackerman

Criterion 3. Agreement of Instantaneous, Colocated Measurements on Several Satellites

Scanner observations	Harrison
Nonscanner observations	Avis

Criterion 4. Spectral Consistency of Three-Channel Scanner Observations from a Single Satellite

Redundancy of Spectrally overlapping, bore-sighted instruments	G. L. Smith

Criterion 5. Agreement of Instantaneous TOA Fluxes Measured by the Scanner and by the Nonscanner

Average inverted scanner data to nonscanner FOV	Green House Wu & Ackerman

TABLE 6. VALIDATION CRITERIA AND RESPONSIBLE INDIVIDUALS (CONCL'D.)

Criterion 6. Satisfactory Checks of Limb Darkening and Bidirectional Models	
Along track data	G. L. Smith
	Brooks
Angular binning of scanner data	Suttles
	Coakley
	Davies
Daily averages of scanner data as a function of viewing zenith	Wielicki
	Green
SAB/MLE on Nimbus-7 ERB data	Wielicki
	Suttles
Criterion 7. Satisfactory Checks of Scene Identification	
V-5 product intercomparisons between ERBE and AVHRR	
Theory	Dieckman
Hybrid bispectral yhreshold	Minnis
Spatial coherence	Coakley
Criterion 8. Satisfactory Checks of Time Averaging	
Data and algorithm check	Hartmann
GOES Time Interpolation	Minnis
	Harrison
METEOSAT time interpolation	Kandel
Criterion 9. Checks against Other Sources of Data	
Radiative transfer tests	Ramanathan
Nimbus 7 ERB check	Kyle
	Vonder Haar
AVHRR OLR data	Gruber
	Miller, Yang
Criterion 10. Reasonableness of Global, Annual Radiation	
Annual cycle	Harrison

TABLE 7. INFLUENCE OF PARAMETERS ON VALIDATION CRITERIA

Parameter	Criterion									
	1	2	3	4	5	6	7	8	9	10
Instrument Parameters										
Scanner Gain	X	X	X	X	O			O	O	O
Scanner Offset	X	X	X	X	O			O	O	O
Nonscanner Gain	X	X	X		O			O	O	O
Nonscanner Offset	X	X	X		O			O	O	O
Inversion Parameters										
Spectra			O	X						O
Scene Model			O	X						O
Scanner Responsivities	O	O	O	X				O	O	O
Correction Matrices		O	O	X	O			O		O
ADM's		O	X		X	X	O	O	O	O
Clear-Sky Radiances						O	X	O		O
Scene Albedos						O	X	O		O
Snow Coverage Maps						O	X	O		O
Averaging Parameters										
Diurnal Albedo Models								X	O	X
Diurnal LW Amplitudes								X	O	X

X denotes major influence

O denotes minor influence

TABLE 8. STATE OF ERBE VALIDATION CRITERIA

Criterion 1. Consistency of Independent Checks of Sensor Calibration

Scanner

$< 0.5\%$ change in 3 years

Nonscanner

Gain tied to solar irradiance better than 0.5%

"Offsets" vary $\approx$ few $W\,m^{-2}$

Criterion 2. Satellite Altitude Agreement of Scanner and Nonscanner on Each Satellite

Average measured differences for 4 validation months

		LW [$W\,m^{-2}$]	SW [$W\,m^{-2}$]
ERBS			
	MFOV	-1	-1
	WFOV	2	-3
NOAA-9			
	MFOV	-1	3
	WFOV	-2	0

Criterion 3. Agreement of Instantaneous, Colocated Measurements on Several Satellites

Scanner gains are equal to $\pm 1\%$

No significant mean bias

Scatter about regression has 1 σ of 5 $W\,m^{-2}$ LW, 15 $W\,m^{-2}$ SW

Criterion 4. Spectral Consistency of Three Channel Scanner Observations from a Single Satellite

Mean discrepancy $< 1\,W\,m^{-2}\,sr{-}1$ for ERBS

Standard deviation 1 to 2 $W\,m^{-2}\,sr{-}1$ for ERBS

Mean discrepancy $\approx 1\,W\,m^{-2}\,sr{-}1$ for NOAA-9 night

Mean discrepancy $\approx 2\,W\,m^{-2}\,sr{-}1$ for NOAA-9 day

TABLE 8. STATE OF ERBE VALIDATION CRITERIA (CONT'D.)

Criterion 5. Agreement of Instantaneous TOA Fluxes Measured by the Scanner and by the Nonscanner

Average measured differences for 4 validation months

		LW [$W\,m^{-2}$]	SW [$W\,m^{-2}$]
ERBS			
	MFOV	-2	-4
	WFOV	5	-1
NOAA-9			
	MFOV	-6	18
	WFOV	2	2

Criterion 6. Satisfactory Checks of Limb Darkening and Bidirectional Models

Along track data
- LW needs $\approx$ 1% more limb-darkening
- SW needs $\approx$ 2% to 3% more limb-brightening, depending on scene, VZ angle, solar zenith

Angular binning of scanner data
- No globally significant biases

Clear Sky Radiances
- LW agrees with theory to $\approx$ 1%
- SW ocean albedos agree with theory to $\approx$ 1% [1% of 0.18]

Viewing Zenith daily averages

Reciprocity
- Good agreement on deserts
- More work may be needed on oceans

SAB/MLE on Nimbus-7 ERB data
- Global biases $< 1\,W\,m^{-2}$ in LW, < 0.005 in albedo
- LW models may need more limb darkening
- SW models may need more limb brightening

TABLE 8. STATE OF ERBE VALIDATION CRITERIA (CONCL'D.)

Criterion 7. Satisfactory Checks of Scene Identification

V-5 Product Intercomparisons between ERBE and AVHRR
Theory, Hybrid Bispectral Threshold, and Spatial Coherence
2/3 of pixels classified correctly
1/3 of pixels not more than one class incorrect
Bias $< 1\,W\,m^{-2}$ in LW
Bias $< 5\,W\,m^{-2}$ in SW

Criterion 8. Satisfactory Checks of Time Averaging

GOES and Meteosat Time Interpolation Check
Monthly Average Regional Error likely to be $\approx 5\,W\,m^{-2}$ or less for SW,
$\approx 2\,W\,m^{-2}$ or less for LW,

Criterion 9. Checks against Other Sources of Data

Radiative Transfer Calculations
$< 1\%$ error in LW at night
AVHRR OLR data
$3\,W\,m^{-2}$ below ERBE LW on global basis
with systematic discrepancies of 5 to $15\,W\,m^{-2}$ in some regions

Criterion 10. Reasonableness of Global, Annual Radiation

Net annual radiation balance estimated $\approx 5\,W\,m^{-2}$
Uncertainty probably about $5\,W\,m^{-2}$

TABLE 9. GLOBAL AVERAGE RESULTS FROM SAB/MLE ANALYSIS OF NIMBUS-7 ERB DATA FOR JUNE 1979

RADIATION BUDGET PARAMETER	SAB METHOD	MLE-ADM METHOD	MEAN DIFFERENCE	RMS DIFFERENCE
INSTANTANEOUS ALBEDO	0.2738	0.2780	0.0042 (1.5%)	0.016 (5.8%)
LW FLUX - DAY	244.3	244.4	0.1 (0.04%)	3.79 (1.6%)
LW FLUX - NIGHT	227.6	228.5	0.9 (0.4%)	3.41 (1.5%)
LW FLUX - TOTAL	235.6	236.3	0.7 (0.3%)	3.09 (1.3%)

TABLE 10. SCENE MISIDENTIFICATION MATRIX

	AVHRR Classification			
ERBE Classification	Clear	Partly Cloudy	Mostly Cloudy	Overcast
Clear	817	161	3	0
Partly	421	1054	314	28
Mostly	12	205	877	878
Overcast	0	4	112	965

Figure 1. ERBE hourly-monthly array. Each month has an appropriate number of days (28, 29, 30, or 31) divided into 24 hourly intervals. Daily averages come from summing data over the hours in each day. These averages are in the right column. Hourly averages come from summing the observations in a column for a particular hour. These hourly averages are placed in the bottom row. The lower right-hand box can then contain either the sum of the daily averages, or the sum of the hourly averages. These last two averages are the grand monthly averages.

Figure 2. Internal calibration stability. These data show the change in the ERBS scanner calibration coefficients required to match observations of the internal calibration sources. The calibration sources are observed about once every two weeks. [*Figure supplied by Robert B. Lee III.*]

Figure 3. Scatter plot of satellite-altitude intercomparisons between the ERBS SW WFOV measurements and the ERBS SW scanner. Each data point represents an average over 32 seconds of nonscanner data and "turned" scanner data.

Figure 4. Scatter plot of simultaneous, colocated ERBS and NOAA 9 scanner fluxes. In these data, the NOAA 9 scanner saw geographic regions within 10 minutes of observations by the ERBS scanner. Each point is a geographic average of the instantaneous fluxes.

Figure 5. Spectral consistency histogram. This histogram shows the frequency of occurrence of values of $\delta_{spectrum}$, which is defined by equation (9). These data were obtained on April 20, 1985, from the ERBS scanner.

Figure 6. Scatter plot of TOA intercomparisons between ERBS SW WFOV measurements and the fluxes from the scanner. Each data point represents an areal average over about 7° of earth central angle.

Figure 7. Normalized limb-darkening from the ERBS along-track scanner observations. As the ERBS passed over the earth, the alongtrack scans observed a given position from several directions. The observations near nadir provided the scene classification, which is "Partly-Cloudy" in this figure. The limb-darkening model for that class produced an equivalent "flux." This flux was divided by the nadir "flux" to produce the normalized values displayed here as a function of viewing zenith angle. The example shown here has radiances that are very slightly more limb-darkened than the model.

Figure 8. Time series of ERBE and GOES observations for the Arizona desert. The observations shown are for April 1985 from the 2.5° × 2.5° region covering the Arizona desert. The regression method of Minnis and Harrison (1984) provided the conversion from the GOES data to TOA fluxes.

Figure 9. Global Map of Reflected Solar Flux for January 1986. This map shows the geographic distribution of reflected solar flux from the combined ERBS and NOAA 9 data. The sun is typically at a latitude of 20° south, emphasizing the reflected sunlight from clouds in this latitude band. Both clouds and snow contribute to the longitudinal features that are clearly visible in the southern hemisphere.

Figure 10. Global Map of Emitted Flux for January 1986. This map shows the geographic distribution of LW flux from the combined ERBS and NOAA 9 data. The high cirrus shields from convective activity over the Amazon and Congo basins and from the Indonesian water continent are major, fixed features of low LW flux.

Figure 11. Global Map of Net Radiative Flux for January 1986. This map shows the geographic distribution of net radiation (absorbed solar flux minus emitted flux) from the combined ERBS and NOAA-9 data. The distribution is surprisingly zonal, with the Sahara standing out as a longitudinal anomaly.

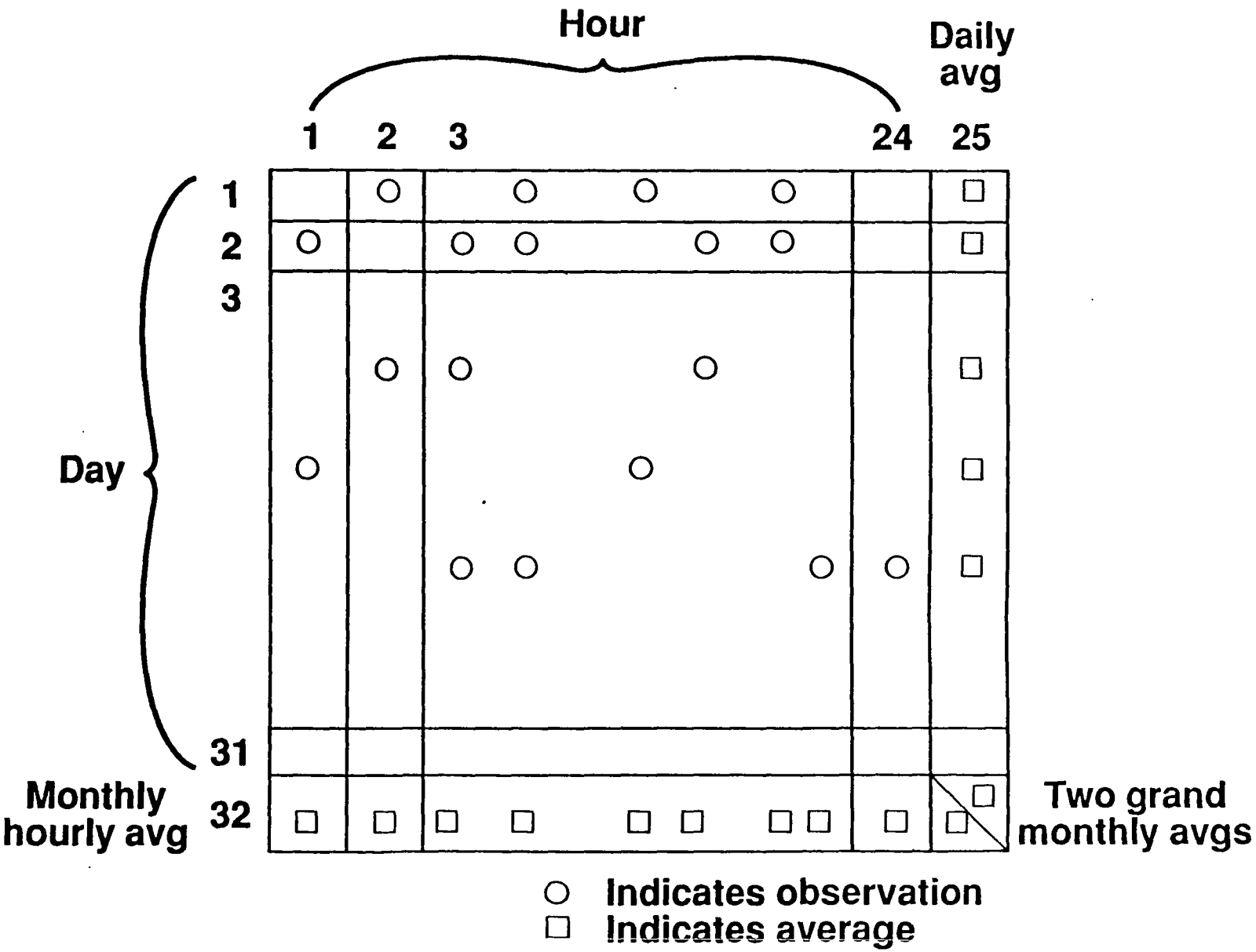
Hour
Daily avg
1
2
3
24
25
Day
1
2
3
31
32
Monthly hourly avg
Two grand monthly avgs
Indicates observation
Indicates average

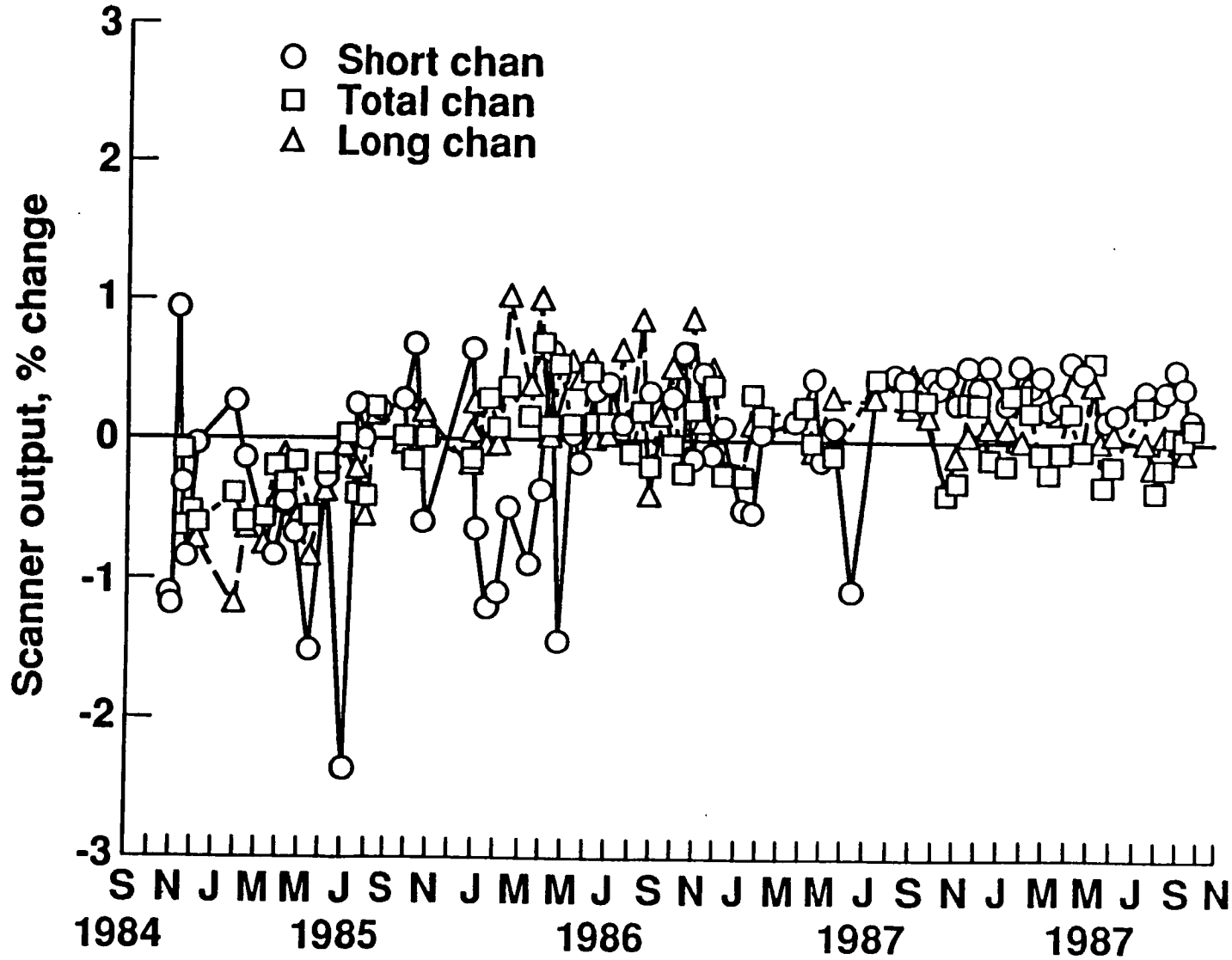
Short chan
Total chan
Long chan
Scanner output, % change
3
2
1
0
-1
-2
-3
S N J M M J S N J M M J S N J M M J S N J M M J S N
1984
1985
1986
1987
1987

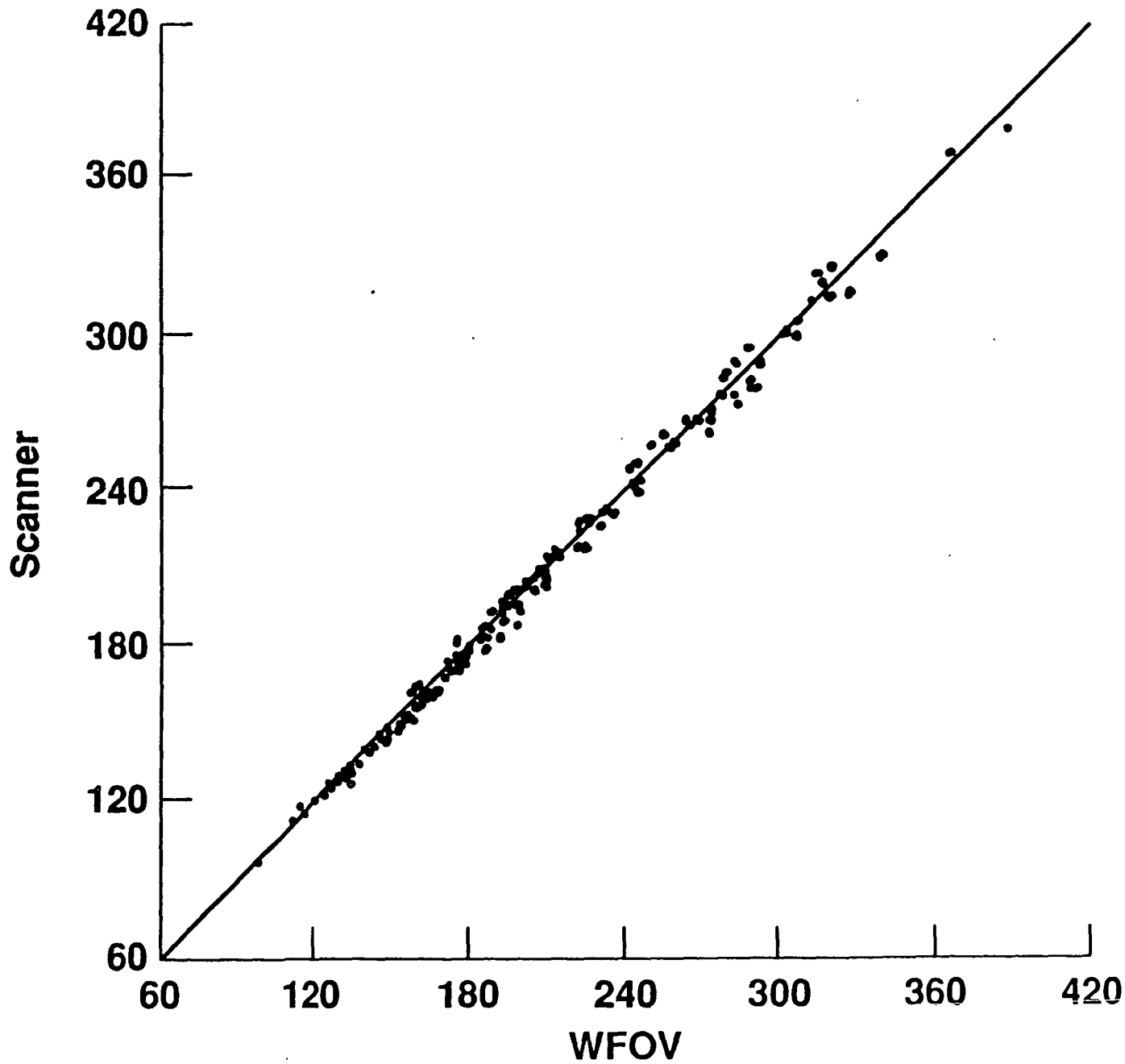
420
360
300
240
180
120
60
Scanner
60
120
180
240
300
360
420
WFOV

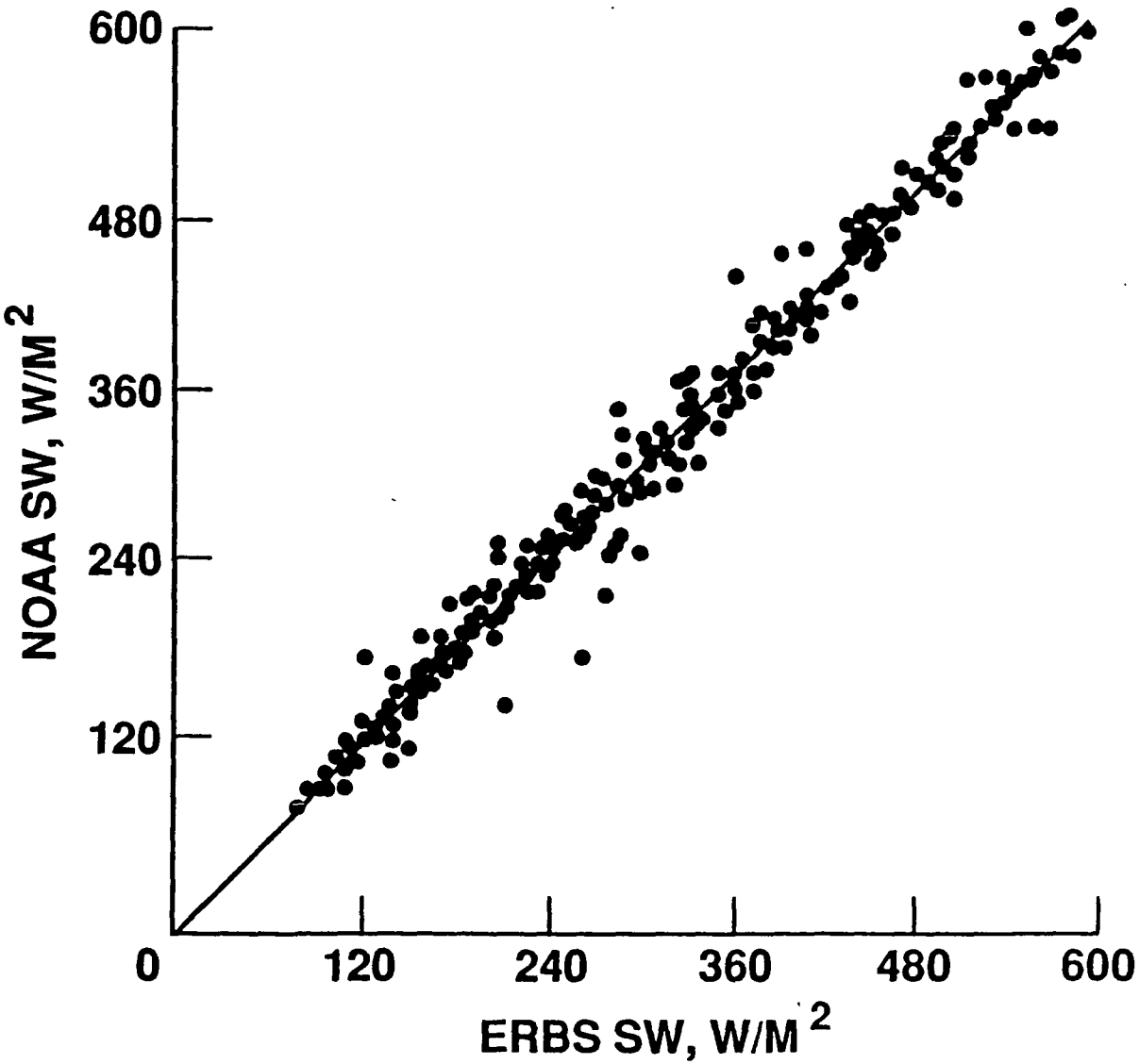
600
480
360
240
120
0
120
240
360
480
600
NOAA SW, W/M 2
ERBS SW, W/M 2

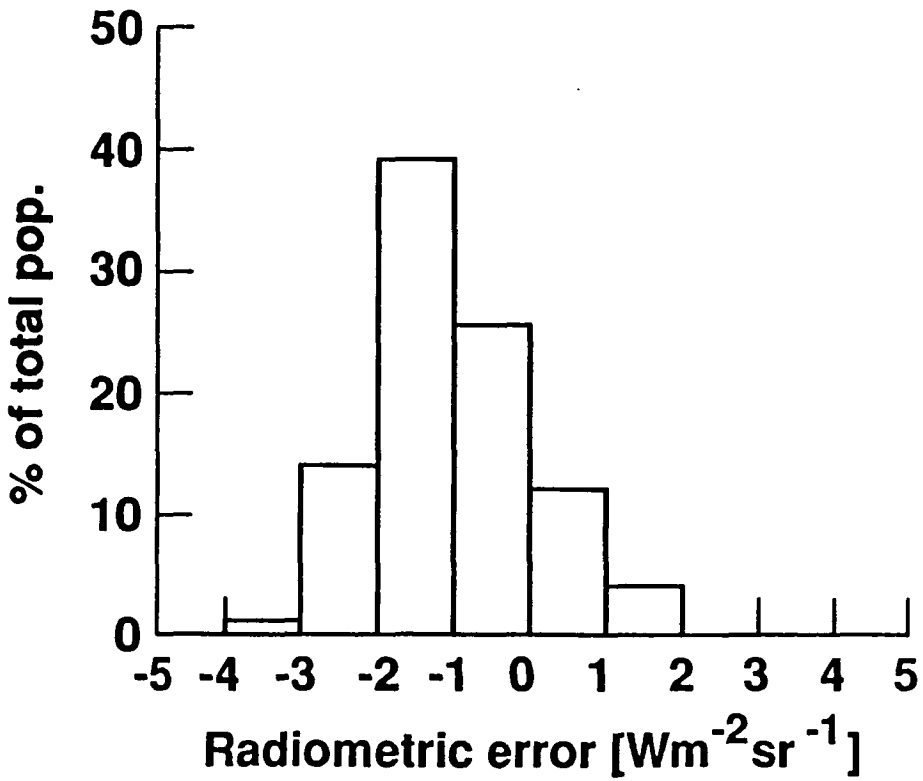
50
40
30
20
10
0
% of total pop.
-5 -4 -3 -2 -1 0 1 2 3 4 5
Radiometric error [Wm-2sr-1]

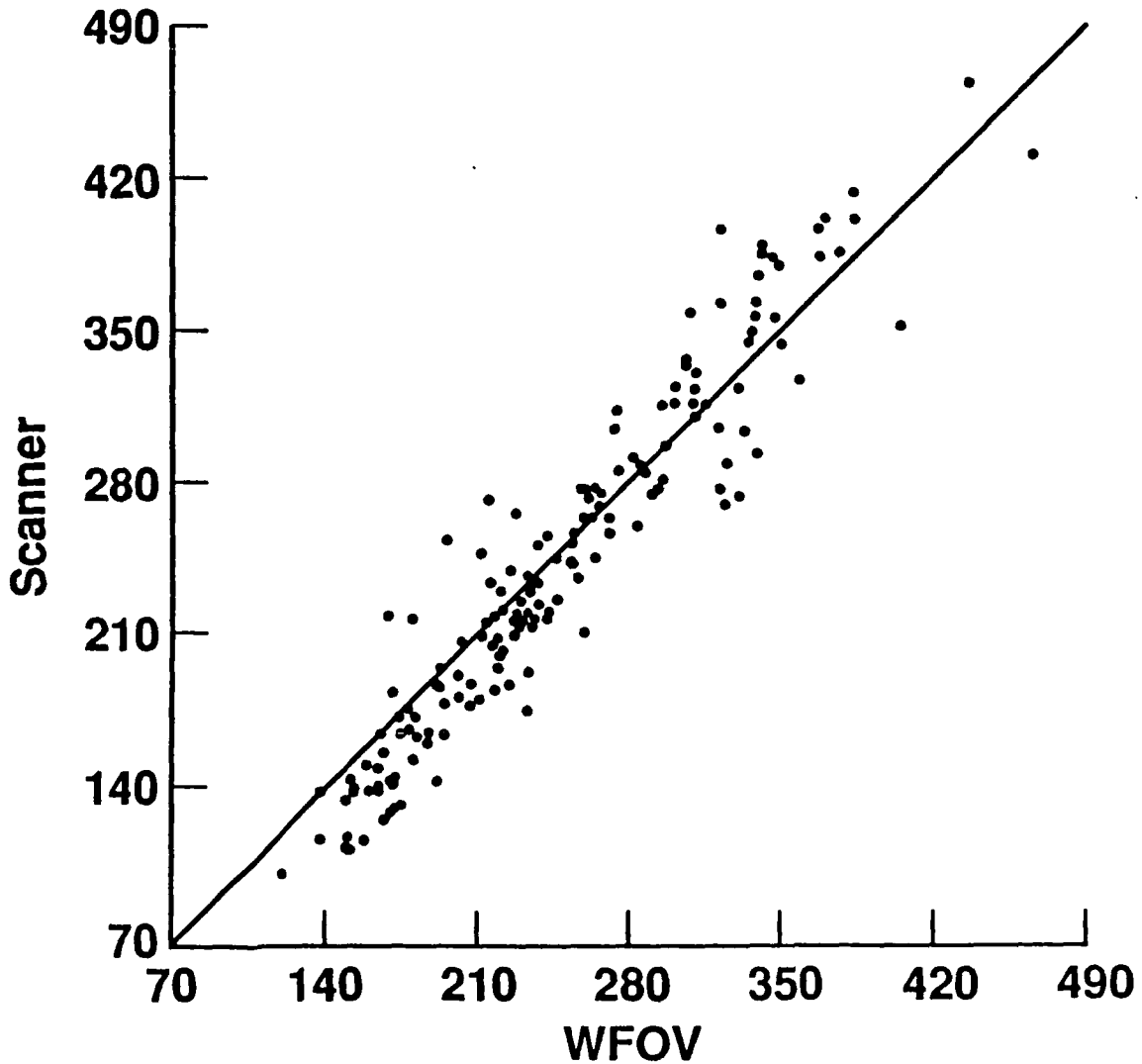
490
420
350
280
210
140
70
Scanner
70
140
210
280
350
420
490
WFOV

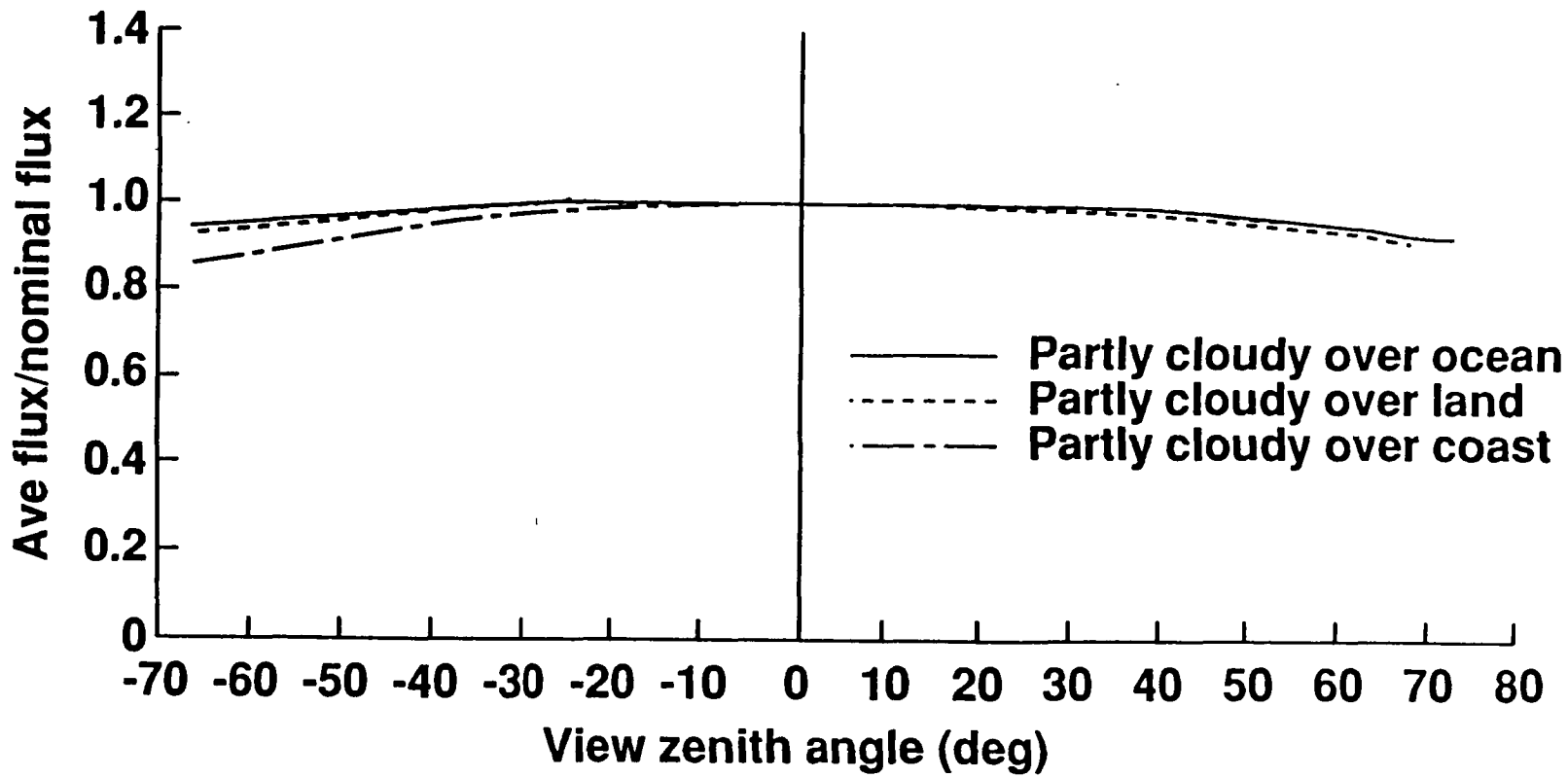
Ave flux/nominal flux
1.4
1.2
1.0
0.8
0.6
0.4
0.2
0
-70 -60 -50 -40 -30 -20 -10 0 10 20 30 40 50 60 70 80
View zenith angle (deg)
Partly cloudy over ocean
Partly cloudy over land
Partly cloudy over coast

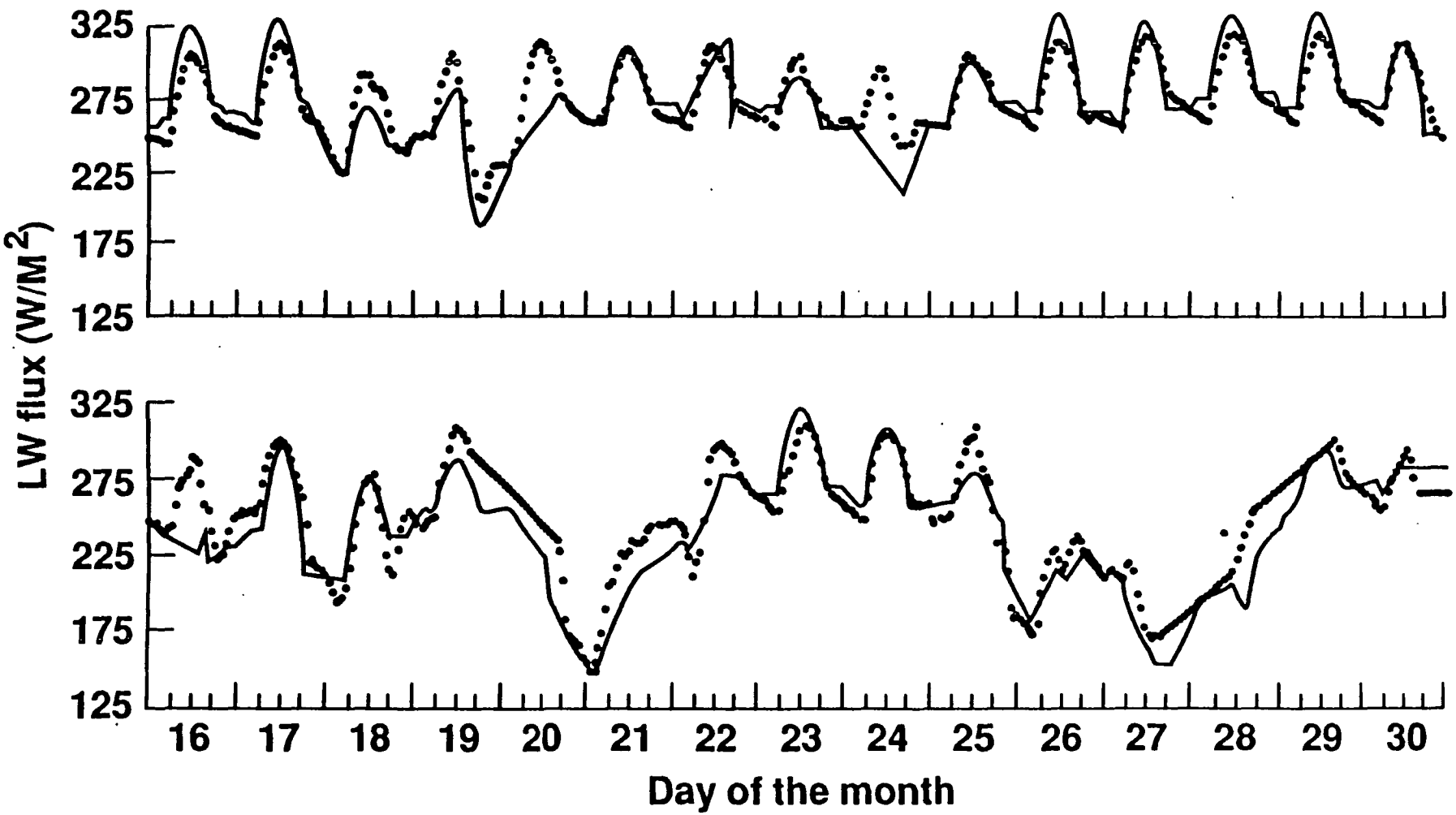
325
275
225
175
125
325
275
225
175
125
LW flux (W/M2)
16
17
18
19
20
21
22
23
24
25
26
27
28
29
30
Day of the month

ORIGINAL PAGE IS
OF POOR QUALITY

ORIGINAL PAGE IS
OF POOR QUALITY

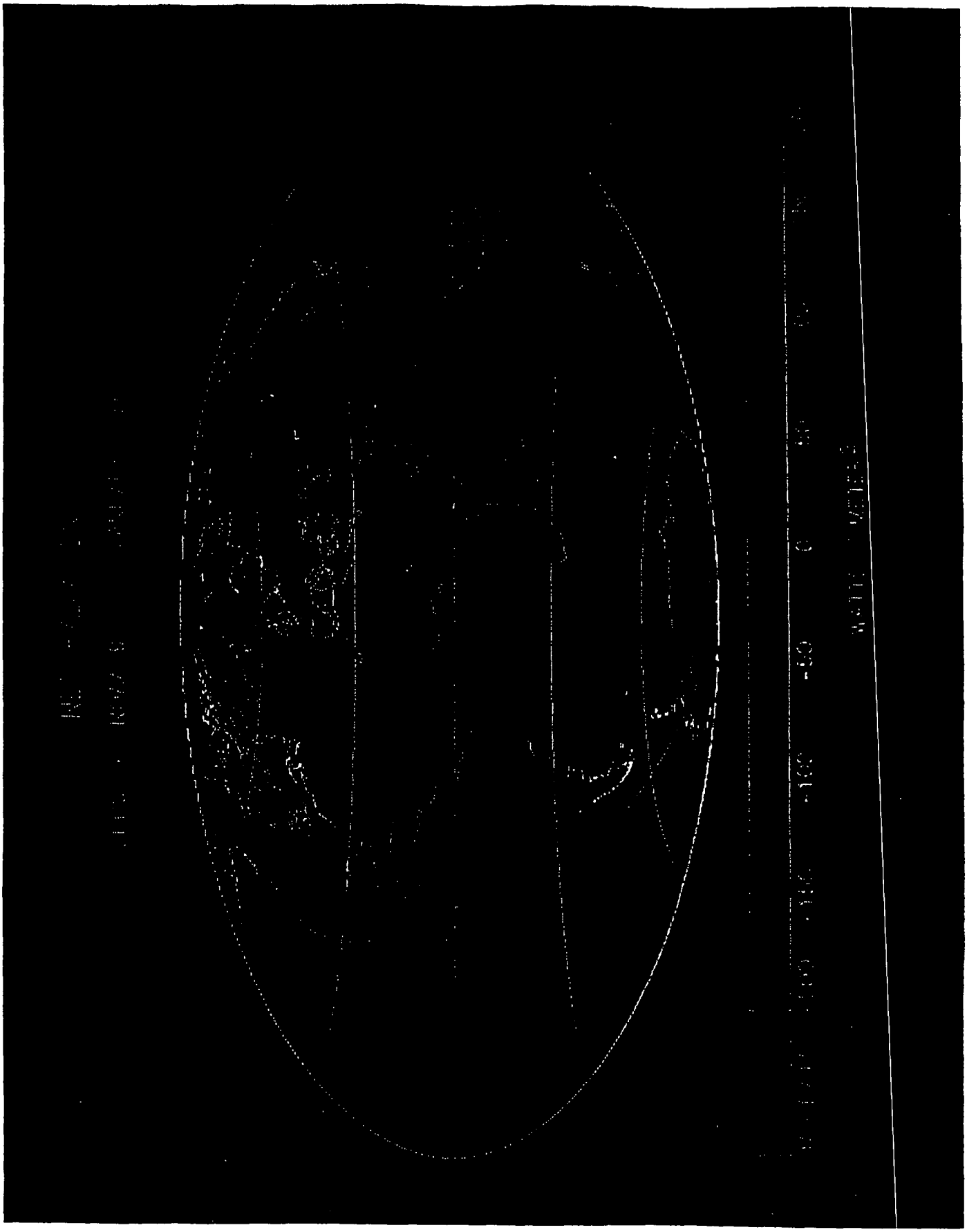

ORIGINAL PAGE IS
OF POOR QUALITY